Structural characterization by Raman hyperspectral mapping of organic carbon in the 3.46 billion-year-old Apex chert, Western Australia

Marie Catherine Sforna, Mark van Zuilen, Pascal Philippot

Structural characterization by Raman hyperspectral mapping of organic carbon in the 3.46 billion-year-old Apex chert, Western Australia

Authors: M.C. Sforna*, M. van Zuilen, P. Philippot

Géobiosphère Actuelle & Primitive, Institut de Physique du Globe de Paris, Sorbonne Paris Cité, Univ Paris Diderot, UMR 7154 CNRS, F-75005 Paris, France

** To whom correspondence should be addressed:*

E-mail: sforna@ipgp.fr, phone: +33(0)1 83 95 77 35

Abstract

The 3.46 billion years old Apex Chert, Pilbara Craton, Western Australia, is well-known for hosting the oldest, highly disputed microfossils on Earth. This rock has a complex history of thermal alteration that includes circulation of hydrothermal fluids, lower greenschist-facies regional metamorphism, and post-metamorphic weathering by meteoric fluids. Carbonaceous material[1] occurs in the sedimentary stratiform part of the chert as well as the underlying intruding hydrothermal black chert veins. In order to identify a least-altered remnant of early life it is necessary to develop a method that enables rapid evaluation of CM structural order on a small spatial scale. Here we present the detailed characterization of CM in the Apex chert by Raman hyperspectral mapping. It is shown that this approach gives better estimates of average Raman band ratios than individual point analyses, and it is demonstrated

[1] *Abbreviations:* CM: Carbonaceous Material

that significant differences in structure exist between CM in the stratiform part of the Apex chert and CM in an underlying black chert vein. The large Raman map-based datasets also reveal that significant mixing took place between these two end members CM's, indicating that the Apex chert has been thoroughly altered by hydrothermal fluid circulation. At the brecciated intersection between the stratiform chert and the intrusive hydrothermal chert vein very poorly ordered CM was found that is not in line with lower greenschist-facies regional metamorphism. It is speculated here that this CM represents an organic fraction that was introduced or thoroughly altered by late stage meteoric fluids. Alternatively, the ubiquitous presence of hematite in this sample caused a perturbation in the Raman spectra of the CM, leading to an artifact in the calculated Raman-based band ratios. Overall it can be concluded that the best preserved CM occurs in the stratiform parts of the Apex chert, while earlier discussions on organic microfossils in this rock often focused on parts of the chert that either represented the hydrothermal veins or the brecciated intersection between the veins and the stratiform part.

1. Introduction

Reconstructing the origin and early evolution of life on Earth is a difficult and controversial task that for a large part is based on rare preserved organic microfossils in ancient chert and carbonate deposits (Brasier et al., 2002, 2005, 2006; Lindsay et al., 2005; Marshall et al., 2011; Olcott Marshall et al., 2012; Schopf et al., 2007 and references therein). As many of these putative fossils occur in hydrothermally-influenced chert deposits, the origin of the CM is questioned (Brasier et al., 2002, 2005; Lindsay et al., 2005). They could represent sedimentary organic debris but could also have been introduced by circulating hydrothermal fluids. Moreover, processes associated with sediment burial such as diagenesis,

secondary hydrothermal fluid circulation, metamorphism, and post-depositional contamination make any unambiguous interpretation of the origin of the CM tenuous. The prolonged effects of temperature, pressure, and strain have altered organic remains to highly aromatic macromolecular structures (kerogen) and ultimately crystalline graphite (Buseck and Huang, 1985; Bustin et al., 1995).

Raman spectroscopy is used since the early seventies for the study of CM as it can rapidly and non-destructively distinguish kerogens from void fillings, modern endolithic organisms, and opaque fluid inclusions. Moreover, it can also probe the degree of structural order of the organic matter and, therefore, be used to estimate the peak metamorphic temperature experienced by the host rock (Aoya et al., 2010; Bernard et al., 2010; Beyssac et al., 2002, 2003; Jehlicka and Beny, 1992; Jehlicka et al., 2003; Lahfid et al., 2010; Rahl et al., 2005; Wopenka and Pasteris, 1991, 1993). Finally, Raman analysis enables imaging of structural heterogeneities on a microscopic scale either inherited from the organic precursor, or formed by secondary processes such as deformation, fluid circulation or adsorption on mineral surfaces (Bustin et al., 1995; Qu et al., 2012; Ross and Bustin, 1990; van Zuilen et al., 2012; Wopenka and Pasteris, 1993). Owing to these different sources of uncertainties, it is therefore of crucial importance that Raman-based interpretations rely on a statistically meaningful dataset. For instance, Aoya et al. (2010) showed that the Raman spectral indicators for structural order of CM can be confidently interpreted only by using the mean value of at least 25 measurements within a single petrographical thin section. It has been shown in studies on CM in meteorites that hyperspectral Raman mapping can be used to generate such large arrays of Raman spectral data (Busemann et al., 2007). This approach has so far not been applied to the description of CMs in metamorphic rocks.

Here we present the application of Raman hyperspectral mapping for the characterization of CM in diagenetically and metamorphically complex Archean terrains. The information in map-based Raman datasets is used to generate a statistically meaningful histogram of band-intensity- and band-area-based indicators of structural order for CM that occurs in a specific region within a rock thin section. Structural characterization is then based on the information in several thousands of spectra instead of a few point-based analyses. We apply this tool to study the structural variation of CM in the Apex chert. This rock has been the focal point for discussions regarding the oldest microfossils on Earth (Brasier et al., 2002, 2005, 2006; De Gregorio et al., 2009; Marshall et al., 2011; Marshall and Olcott Marshall 2011; Olcott Marshall et al., 2012, 2013; Olcott Marshall and Marshall, 2013; Pinti et al., 2009, 2013; Schopf, 1993; Schopf et al., 2002; Schopf and Kudryatsev, 2012, 2013; Schopf and Packer, 1987). The controversy still exists regarding the distinction between primary sedimentary CM and hydrothermally-derived fractions of CM. Our samples are derived from the bedded part of the formation as well as from the strongly brecciated and hydrothermally-influenced feeder vein (Fig. 1). An overview is given of the different ways in which Raman spectral indicators for CM structure can be calculated and which one use when peak metamorphism has reached only lower greenschist-facies. The application of Raman hyperspectral mapping to obtain large datasets is also discussed. Finally, an assessment of the variations in CM structural order within some key regions of the Apex chert is provided.

2. Theory: the Raman spectrum of carbonaceous material

A Raman spectrum of sedimentary CM is composed of a first-order region (1100-1800 cm^{-1}) and a second-order region (2200-3400 cm^{-1}). In an infinite structure such as pure crystalline graphite, only the G-band (~1580 cm^{-1}) is Raman active (Tuinstra and Koenig,

1970). It results from the vibration of the E_{2g} mode of sp^2-bonded hexagonal ring structures. The vibration of the A_{1g} breathing mode of sp^2 rings becomes possible if the in-plane crystal domain size (L_a, in Å) of individual graphene layers within the crystal is limited by defects, *e.g.* in micro-crystalline graphite or in disordered CM. This gives rise to the additional D-bands (D for disorder) at ~1350 cm^{-1} (D1) and at ~1620 cm^{-1} (D2) (Fig. 2a). Many out-of-plane defects, related to tetrahedrally coordinated carbons, dangling bonds and hetero-atoms, occur in natural CM. These heterogeneities give rise to a broad D3-band at ~1500 cm^{-1} (Beyssac et al., 2002; Wopenka and Pasteris, 1993). When the crystallinity of the organic matter is very low, a shoulder can be observed on the D1-band at ~1190-1250 cm^{-1} (Lahfid et al., 2010; Sadezsky et al., 2005). This band (D4) has been tentatively attributed to sp^2-sp^3 bonds or C-C and C=C stretching vibration of polyene-like structure (Dippel and Heintzenberg, 1999). The bands for the second order are located at ca. 2700, 2900 and 3200 cm^{-1}. They are attributed to overtone (2700 cm^{-1}: 2xD1, 3200 cm^{-1}: 2xD2) or combination modes (2900 cm^{-1}: G+D) (Sadezsky et al., 2005).

Natural CMs are classically characterized by analysis of the first-order spectrum. Since there is considerable overlap between the different disorder-related bands, different protocols exist for band assignment and spectral profile fitting. A commonly used protocol assigns a single D-band at ~1350 cm^{-1} and a G-band at ~1600 cm^{-1} (Bonal et al., 2006; Busemann et al., 2007; Ferrari and Robertson, 2000; Marshall et al., 2007; 2001; Olcott-Marshall et al., 2012; Quirico et al., 2003; Wopenka and Pasteris, 1993). From the intensity ratio of these D- and G-bands the degree of structural order of CM can be determined. In chemically pure graphitic materials a general inverse correlation is observed between in-plane crystal domain size L_a (Å) and the intensity-based I_D/I_G-ratio (Tuinstra and Koenig, 1970) or area-based A_D/A_G-ratio (Larouche and Stansfield, 2010). However, when very poorly ordered CMs are considered, this relationship becomes inaccurate. Several other parameters have

118 therefore been used to describe the degree of maturation in such materials, including D-width
119 (FWHM-D), G-width (FWHM-G), D-position, and G-position (Bonal et al., 2006; Busemann
120 et al., 2007; Ferrari and Robertson, 2000; Kelemen and Fang, 2001; Quirico et al., 2003). The
121 most sensible way to study the maturity of poorly organized CM is to look at the width of the
122 D- and G-band in function of their intensity ratio. When poorly ordered CM is progressively
123 metamorphized, the width of the D-band and the one of the G-band decrease as I_D/I_G
124 increases. Here, we will use the widths ratio FWHM-D/FWHM-G in order to trace CM
125 maturity.

126 When CM is poorly ordered, another common protocol decomposes the D- and G-
127 bands into the individual D1-, D2-, D3-, D4- and G-bands (Aoya et al., 2010; Bernard et al.,
128 2010; Beyssac et al., 2002; Lahfid et al., 2010). From this band assignment several ratios can
129 be calculated that describe the structural order of natural CMs. As the overall process of
130 alteration and graphitization is non-reversible, studies of metamorphosed organic matter have
131 shown that such ratios faithfully record peak-metamorphic temperatures (Beyssac et al., 2002;
132 Lahfid et al., 2010; Rahl et al., 2005; Wopenka and Pasteris, 1993). Beyssac et al. (2002)
133 defined the ratio R_2 (1) and using progressively altered CMs in metapelites they were able to
134 determine a relationship (2) with peak metamorphic temperature in the range 330°-650°C.

135

136 $$R_2=A_{D1}/(A_{D1}+A_{D2}+A_G) \quad (1) \quad \text{with } T= - 445 * R_2 +641 \ (\pm 50°C) \quad (2)$$

137

138 Above 650°C, CM has attained the triperiodic structure of pure graphite and R_2 has
139 virtually vanished. In very low-grade metamorphic terrains (T-range between 200° and
140 330°C), CMs display a broad D1-band, significant D4- and D3-bands, and a relative intense
141 G-band. For this range Lahfid et al. (2010) defined the ratios R_{A1} (3) and R_{A2} (5) and
142 determined relationships (4, 6) with peak metamorphic temperature:

$R_{A1}= (A_{D1}+A_{D4}) / (A_{D1}+A_{D2}+A_{D3}+A_{D4}+A_G)$ *(3)* with $R_{A1}=0.0008T$ (°C ± 50) + 0.3758 *(4)*

$R_{A2}= (A_{D1}+A_{D4}) / (A_{D2}+A_{D3}+A_G)$ *(5)* with $R_{A2}=0.0045T$ (°C ± 50) + 0.27 *(6)*

The intensity of the D4- and D3-bands can also be very useful as the decrease of these bands relative to D1 is linked to an increase in structural order. Accordingly, we define two simple ratios that describe the degree of structure in poorly ordered CMs:

$R_{D3}=I_{D3}/I_{D1}$ *(7)*

$R_{D4}=I_{D4}/I_{D1}$ *(8)*

It is important to note that all these parameters and ratios can only properly describe CMs that originate from a common precursor and have experienced the same conditions of maturation. Certain spectral parameters are calibrated as a structural indicator using a specific group of CMs (e.g. a coal series) or a specific type of rock matrix (e.g. metapelites). In natural systems, however, CMs often have an unknown precursor or can represent a mixture of different precursors (Behar et al., 2008; Barker, 1996; Waples, 1994). Moreover, many CMs occur in rocks that have highly complex metamorphic histories. In the present paper a type of CM is described that has been the focus of controversy, since the precursor has been interpreted as remnant cyanobacteria (Schopf and Packer, 1987), methanogens (Ueno et al., 2004), or the products of Fischer-Tropsch synthesis (Brasier et al., 2002, 2005, 2011; Lindsay et al., 2005). It is thus arbitrary what exact spectral parameters and ratios are used to describe the variation in structure in this CM. We therefore decided to apply two different but widely

168 used band-fitting protocols and to calculate the full range of spectral parameters and ratios.
169 Since the CMs in this study occur in chert matrix, a direct comparison with metapelite-based
170 geothermometers R_{A1}, R_{A2}, R_2 is not possible. We use these ratios as indicators of structural
171 order, but only calculate 'tentative' peak-temperatures.
172

173 ## 3. Geological setting and sample description

174

175 ### 3.1 Regional geology

176

177 The East Pilbara Granite-Greenstone Terrane (Fig. 1), located in Western Australia,
178 represents a continental volcanic plateau consisting of granitoid complexes embedded in the
179 greenstone belts of the Pilbara supergroup that formed between 3.72 and 2.85 Ga (van
180 Kranendonk et al., 2002). It represents one of the three ancient crustal nuclei of the Pilbara
181 Craton within the West Pilbara Granite-Greenstone Terrane and the Kurrana Granite-
182 Greenstone Terrane (for further details see van Kranendonk et al., 2002; van Kranendonk,
183 2006). Some of the oldest and best preserved Archean rocks on Earth can be found in the
184 3.515 and 3.427 Ga Warrawoona group, within the lower part of the East Pilbara stratigraphy
185 (van Kranendonk, 2006). It consists of a thick section of dominantly basaltic rocks
186 intercalated with subordinate felsic volcanic rocks (tuffs and flows), hydrothermal barite and
187 sulfide deposits, and cherty metasedimentary rocks including carbonate and jasper deposits
188 (van Kranendonk and Pirajno, 2004). Metamorphic conditions range from prehnite-
189 pumpellyite to greenschist facies (Brasier et al., 2005; van Kranendonk, 2006).

190 The 3.46 Ga old Apex Basalt Formation, which forms the middle section of the
191 Warrawoona Group, is composed mainly of komatiitic basalts with minor amounts of
192 tholeiitic basalts, dolerite flows and dikes (van Kranendonk, 2000). The formation shows
193 evidence of submarine volcanism, including chilled margins, hyaloclastic breccias, and pillow
194 basalt textures. The Apex Basalt Formation is divided into three structural blocks (North,
195 Central and South), which are limited by syn-sedimentary fault systems (Brasier et al., 2005).
196 The Apex chert (Fig. 1b), located near Marble Bar in the Chinaman Creek Area, is one of the
197 chert horizons that occur in these blocks. It consists of white and black stratiform chert up to
198 25 m thickness. The bedding is defined by moderate to good local sorting and orientation
199 which testify to a primary sedimentary origin (Brasier et al., 2005). Results from mapping
200 showed that these stratiform cherts were fed by individual swarms of black chert veins that
201 were attributed to a stage of pervasive hydrothermal fluid circulation attending the deposition
202 of the stratiform sedimentary chert (Brasier et al., 2002, 2005; Nijman et al. 1998).

203 The contact between the black chert veins and the stratiform chert is marked by
204 strongly brecciated material composed of angular fragments of both stratiform chert and black
205 chert veins within a white to translucid secondary chert matrix of likely secondary
206 hydrothermal origin (Brasier 2002, 2005, 2011; van Kranendonk, 2006). Both the bedded
207 chert and black chert veins are cut across by numerous secondary quartz veins that formed
208 during a later regional metamorphic overprint. Similar stratigraphic relationship between
209 stratiform sedimentary chert and intrusive black chert veins were recognized on a regional
210 scale in the different formations forming the Warrawoona Group (van Kranendonk, 2006).

211 Some of the oldest carbonaceous microstructures resembling fossilized bacteria were
212 reported in the black chert (Schopf and Packer, 1987; Schopf, 1993). At the time of discovery,
213 the origin of the chert was thought to be sedimentary and represent a shallow marine

depositional setting in which photosynthetic bacteria could thrive (Schopf and Packer, 1987). Brasier et al. (2002, 2005) have subsequently shown that the samples studied by Schopf et al. (2002) were derived from a feeder black chert vein representing a conduit for silica-rich hydrothermal fluids. A study based on Si isotopes confirmed that the Apex stratiform chert was derived from seawater silica rather than hydrothermal silica (van den Boorn et al., 2007). In contrast, the silica in the black chert veins precipitated from hydrothermal fluids upon cooling and/or mixing with seawater at depth (van den Boorn et al., 2007). It is highly unlikely that photosynthetic organisms occurred in such a sub-seafloor hydrothermal setting. Rather, it has been suggested that CM was produced abiogenically by Fischer-Tropsch synthesis (Brasier et al., 2002; De Gregorio and Sharp, 2003, 2006a, 2006b) or by partial decomposition of iron carbonate (Garcia-Ruiz et al., 2003). As Lindsay et al. (2005) suggested, the abiotic organic output of such systems may overwhelm the signatures of primitive life and therefore makes it the most difficult environment in which to recognize a record of the early biosphere. Alternatively, it has been proposed that the 3.5 Ga subseafloor hydrothermal system was inhabited by chemoautotrophic organisms (Ueno et al., 2004), sulphur bacteria (Wacey et al., 2011), and/or hyperthermophile bacteria (Brasier et al., 2002; De Gregorio et al., 2009).

It should be stressed that the different rock types forming the Apex Formation have been influenced by multiple episodes of hydrothermal circulation, regional metamorphic overprint and by various extent of weathering alteration, complicating the alteration history of the organic material. Low degree of alteration primarily induced by peak regional metamorphism is expected in the stratiform chert while a more intense thermal alteration induced by hydrothermal activity is expected in and near the feeder black chert veins. The late

237 stage meteoric alteration may have also affected the overall structure of the original
238 carbonaceous material.

239

240 **3.2. Sample description**

241

242 A total of six samples (sampled in 2002 and 2004) from different parts of the Apex
243 chert (Fig. 3) were selected for analysis. These include: three samples of black chert veins
244 (#1, #2 and #6), one from the brecciated zone at the intersection between the stratiform chert
245 and black chert vein (#3), and two from the stratiform chert (#4, #5). All these samples are cut
246 across with white quartz veinlets of secondary origin. Mineralogy was determined by optical
247 microscopy and Raman spectroscopy on polished thin section. Sample #1 consists mainly of
248 quartz with minor amounts of randomly distributed CM. The different colors of the matrix are
249 due to the relative amount of CM, the black chert being richer in organic matter than the gray
250 chert. Sample #2 represents an altered green-glassy tuff that has been pervasively silicified by
251 hydrothermal fluids. Sample #3 consists of small blocks of fractured stratiform chert
252 composed of quartz, CM, hematite, anatase and minor goethite, embedded in a matrix of
253 black chert composed of quartz, CM and minor hematite, goethite, anatase and pyrite.
254 Samples #4 and #5 are stratiform cherts consisting of alternating bands of CM-rich (black)
255 and CM-poor (white, gray) cherty material with minor hematite, goethite, anatase, and pyrite.
256 Sample #6 consists mainly of dark chert with a small amount of CM dispersed in a matrix
257 mainly composed of quartz and minor anatase. This phase is cut across with a white chert.
258 Based on this petrographic description a distinction is made here between CM associated with

stratiform chert (Fig. 3, white dots) and CM associated with hydrothermal chert (Fig. 3, black dots).

4. Methods

4.1 Spectral acquisition

All Raman analyses were performed with a Renishaw In Via Raman spectrometer coupled to an Olympus BX61 confocal microscope and with an Ar-ion-20 mW monochromatic 514 nm as laser source. Laser excitation was adjusted to an on-sample intensity of *ca.* 2 mW (measured with a Coherent Lasercheck Analyser) and focused through a 50x objective to obtain a 1-2 µm spot size. Acquisitions were obtained with a 1800 l/mm grating and 100 cm^{-1} cut-off edge filter, in 'Streamspot'-mode with an air cooled (-70°C) 1024x256 pixel CCD array detector. This method enabled a 2000 cm^{-1} spectral detection range. Beam centering and Raman spectra calibration were performed daily on a Si-Al microprocessor chip with a characteristic Si Raman band at 520.4 cm^{-1}. A 1 s static mode analysis (fixed at 520 cm^{-1}) was used to tune the focal plane position and optimize the count rate. Point analysis measurements were made in static mode (fixed at 1150 cm^{-1}) for 2x10 s running time and in extended mode for 1x10 s over a 100-4000 cm^{-1} range. Raman hyperspectral maps were acquired in 'Streamspot' static mode fixed at 1150 cm^{-1}, with a motorized Prior Stage allowing XYZ displacement with step precision better than 1 µm. Each spectrum was acquired at 1x9 s running time.

A total of 87 spectra have been acquired by punctual analysis for the 6 samples (19 for #1, 11 for #2, 16 for #3, 13 for #4, 14 for #5 and 15 for # 6). Eight maps have been acquired (squares on Fig. 3), one for each sample with the exception of samples #1 and #6, for which two maps have been obtained (see ST1). A total of 33,813 individual spectra have been collected. Spectra obtained by hyperspectral mapping have lower resolution than punctual analysis. In order to obtain good estimation for the calculated ratios, we excluded the spectra in which the intensity of the D1-band was less than 10,000 counts. Moreover, spectra for which one or more of the assigned bands could not be fitted were excluded. Overall, 7,296 spectra have been considered in this study (n#1= 3994, n#2= 101, n#3= 1758, n#4=1225, n#5= 101, n#6-1=23, n#6-2=82).

4.2 Spectral decomposition

The recorded spectral data were treated with the software 'Renishaw Wire 3.3'. The baseline due to the background fluorescence must be removed and the 5 bands of the spectrum must be fitted in order to determine the different spectral parameters (height, area, full-width at half maximum (FWHM)) for quantitative description of the CM structure, (Lahfid et al., 2010; Sadezsky et al., 2005). The baseline was subtracted by third order polynomial fit. We performed the subsequent peak fitting and characterization by band decomposition based on a Gaussian-Lorentzian function with 10,000 iterations per fit. For comparison with literature data and discussion of the various aspects of CM structural order, we followed two different band-fitting protocols; 1) D1-, D2-, D3-, D4- and G-bands are decomposed (Sadezky et al. (2005) and Lahfid et al. (2010)) (Fig. 2a), and 2) only D- and G-bands are taken into account (Bonal et al. 2006; Ferrari and Robertson, 2000; Olcott Marshall et al., 2012; Quirico et al., 2003; Wopenka and Pasteris, 1993) (Fig. 2b). In the first protocol,

the band positions were constrained to lie between 1340-1360 cm^{-1} for D1, 1615-1625 cm^{-1} for D2, 1490-1510 cm^{-1} for D3, 1150-1250 cm^{-1} for D4 and 1580-1610 cm^{-1} for G (Fig. 2a). These intervals are based on the mean values given by Sadezky et al. (2005). In addition, the intensity of D2 was constrained to be less than half of that of the G-band. For the D4 band, the FWHM was limited at a maximum of 200 cm^{-1} in agreement with the interval of FWHM determined for D4 by Sadezsky et al. (2005). These constraints were necessary to assure proper band assignment by the fitting software. The same fitting procedure was applied to the Raman hyperspectral map arrays. In the second protocol the band positions were constrained between 1340-1360 cm^{-1} for D and 1580-1610 cm^{-1} for G (Fig. 2b).

4.3. Artifacts due to sample polishing

Polishing of rock thin sections can induce damage in the CM structure and therefore have a strong influence on the resulting Raman spectra (Beyssac et al., 2003; Mostefaoui et al., 2000; Nasdala et al., 2003; Nemanich and Solin, 1979; Pasteris, 1989; Wang et al., 1989; Wopenka and Pasteris, 1993). To avoid this problem it has been proposed that measurements should be performed on chemically isolated CM (Wopenka and Pasteris, 1993), freshly cracked surfaces (Tice et al., 2004), or by focusing the laser beam on CM grains embedded in a transparent mineral matrix below the surface of a petrographic thin section (Beyssac et al., 2003; Lepland et al., 2011; Nasdala et al., 2003). However, several studies have shown that polishing has little damaging effect on organic matter displaying R_2 ratio $\geq$ to 0.5 (Beyssac et al., 2003; Qu et al., 2011, 2013). To determine the magnitude of polishing artifacts on the Apex chert samples, we performed a specific test on samples #1, #4 and #5. Based on the

328 standard deviation (2σ), the Raman spectrum parameters of sub-surface CM structures that are
329 fully embedded in the quartz matrix are exactly similar to that of the polished CM structures
330 (Table 1). Based on this observation, we conclude that CM in the Apex chert can be directly
331 studied by surface Raman analysis, and thus that Raman hyperspectral maps reflect real
332 variations in CM structures.

333

334 **4.4. Artifacts from laser-induced heating**

335 CM is very sensitive to laser-induced heating that can provoke severe damages
336 (Everall et al., 1991; Kagi et al., 1994). It leads to a downward shifting for the G- and D-
337 bands. It is possible to prevent these effects with the use of low level laser (<5mW, Beyssac et
338 al., 2003; Everall et al., 1991). We used a 2mW laser intensity, which is comparable with or
339 lower than that used in other Raman spectroscopy-based studies of CM in greenschist-facies
340 metamorphic grade rocks (Lepot et al., 2013; Olcott-Marshall et al., 2012; Tice and Lowe,
341 2004; Wopenka and Pasteris, 1993). In addition, Qu et al., (2013) specifically tested the effect
342 of laser heating for intensities up to 5 mW on the surface of CM-rich rocks of the greenschist-
343 facies Zaonega Formation, Russia, and found no evidence of thermal damage.

344

345 **5. Results and discussion**

346 The average Raman band characteristics and calculated band ratio are listed for all
347 samples in Table 2. Individual spectral data are listed in the Supplementary Data (ST3).
348 Protocol 1 was used to enable the calculation of the ratios R_{D3}, R_{D4}, R_{A1}, R_{A2}, and R_2, while
349 protocol 2 was used to obtain the ratios I_D/I_G, A_D/A_G, and the positions and widths of the D-
350 and G-bands. In order to provide a complete set of Raman characteristics the positions and

351 widths of the decomposed D1- and G-bands from protocol 1 are also reported. The mean
352 values of the map-based ratios slightly differ from those calculated from punctual analyses
353 (Table 2). Hyperspectral maps derived-ratios have smaller standard deviation leading to a
354 better estimation of the calculated ratio and thus of the ordered/disordered state of the CM in
355 the Apex chert.

356 All Raman spectra (from point analysis and hyperspectral maps, Fig. 4 and S1,
357 respectively) obtained in this study display well-developed D3 and D4 bands, and have a D1
358 band (FWHM < 70 cm^{-1}) that is more intense than the G band. These spectral characteristics
359 are indicative for rather poorly ordered CM that is typically encountered in lower greenschist-
360 facies Archean terrains (Lepot et al., 2013; Marshall et al., 2007). The spectra of the CM from
361 the brecciated chert (Fig. 4 f, S1f) are also typical of low-ordered CM. However, the intensity
362 of D1 is nearly the same as that of the G-band, D1 is wider (FWHM= 96 ± 22 cm^{-1}), and D3 is
363 higher than for the other samples. All spectra of punctual analyses display well-developed
364 second order bands (Fig. 4). This observation differs from that of Olcott Marshall et al.
365 (2012), in which a secondary phase is described that does not contain bands in the second
366 order spectrum.

367

368 **5.1. CMs in stratiform cherts (#4, and #5) vs CMs in black chert veins (#1)**

369 Some important spectral differences are observed between CMs from the stratiform
370 chert and CMs from the black chert vein. CM spectra for black chert vein (Fig. 4 a-c, Fig. S1
371 a-c) have always a narrower D1-band (55-60 cm^{-1}) than CM spectra of the stratiform chert
372 (Fig.4 d-e, S1de, 64-67 cm^{-1}). Moreover, black chert vein spectra display less intense D3- and
373 D4-bands (Fig. 6).

A distinction between the stratiform chert CM (#4, #5) and the black chert vein CM (#1) is also observed in several of the calculated Raman spectral ratios (Table 2).This is most clearly seen when R_2 is plotted against I_D/I_G (Fig. 5a). Samples #4 and #5 display lower I_D/I_G and R_2 ratios than sample #1. Since R_2 decreases with increasing degree of order in the CM, lower R_2 ratios for the stratiform chert CM imply that the CM is more organized than that of the black chert veins. However the spectra of the stratiform cherts have a lower R_{A1} and I_D/I_G than those of the black chert veins (Fig. 5b). Since R_{A1} increases with increasing degree of order (Lahfid et al., 2010), lower R_{A1} values are in agreement with a more disordered CM in the stratiform cherts.

This apparent contradiction can be explained if the structural order of these CMs covers the upper limit of the R_{A1} ratio (Lahfid et al., 2010) and the lower limit of the R_2 ratio (Beyssac et al., 2003). In metapelitic rocks this would correspond to peak metamorphic temperatures that range from slightly below to slightly above 330°C. The R_{A1} and R_2 ratios are therefore not well suited to estimate the degree of organization of CM in these rocks. The ratio I_D/I_G is also problematic, since it increases with increasing structural order until a certain maximum is reached, and then decreases with increasing structural order until the D-band is absent (Busemann et al., 2007; Ferrari and Robertson, 2000). Stratiform cherts CMs have lower I_D/I_G ratios that black chert CMs (Fig. 5a-b), and it is not clear whether this reflects a higher or lower degree of structural order. The only effective indicators are then the positions and widths of the D- and G-bands, or – in case of total decomposition of the first-order spectrum – the presence of the specific disorder-related bands D3 and D4. The FWHM of the D1 band and the intensities of the D3 and the D4 bands are significantly higher in the CM spectra of the stratiform cherts (Fig. 6a-b) than in those of the black chert veins. As shown in Figure 6c, the stratiform chert CM displays high R_{D3} and R_{D4} ratios of 0.10 and 0.09

398 respectively, which correspond to a low structural order. In contrast, the black chert vein CM
399 have lower R_{D3} and R_{D4} ratios of 0.06 and 0.06, respectively, which are indicative of an
400 higher structural order. FWHM-D, R_{D3} and R_{D4} are then in good agreement, and indicate that
401 the CM in the stratiform cherts is more disordered than that in the black chert veins.

402 While the punctual analyses reveal two distinct CMs within the samples #1, #4 and #5,
403 the large datasets of the hyperspectral maps show a considerably more complex situation. The
404 modes of the normalized histograms for R_{D3} ratio are different for sample #1 and #4/5 (Fig. 7)
405 in line with two populations of CM, but a considerable overlap between the population is
406 observed as well. The non-gaussian distributions of the different calculated ratios (normality
407 tested with the Kolmogorov-Smirnov test) show an asymmetry in the low values of RD3 for
408 samples #4/#5 and in the high values of RD3 for sample #1(Fig. 7a). These asymmetric
409 distributions could reflect the preservation of a primary phase in the black chert despite the
410 influence of hydrothermal fluids and the influence of the hydrothermal fluids that crossed the
411 stratiform chert. There is thus no distinct separation between CM types, but rather a
412 continuum of mixed CM components. On average, the most altered CM particles occur within
413 the deep regions of the hydrothermal black chert veins whereas the least altered are preserved
414 in the stratiform cherts. This suggests either that there was a significant difference between
415 the organic precursors in the deep hydrothermal veins and the organic precursors in the
416 stratiform chert, or that CM in the hydrothermal fluids experienced a higher peak temperature
417 then the CM in the stratiform chert.

418

419 **5.2. Sample-scale heterogeneities in sample #6**

The Raman hyperspectral maps enable the characterization of sample-scale structural heterogeneities. This is most clearly seen in the spectral data of sample #6. Two maps have been obtained for sample #6; one in the dark grey chert (#6-1, Fig. 3f) and one in the secondary cross-cutting white chert (#6-2, Fig. 3f). The map-derived R_{D3} and R_{D4} values for the darker chert are in the range of the stratiform cherts (0.08 and 0.09, respectively; Fig. 7b). The map-derived ratios in the white chert portion of the thin section are lower (0.06 and 0.07, respectively) and fall in the range of black chert veins (Fig. 7b). They could therefore reflect an episode of channeled hydrothermal fluid infiltration within the stratiform cherts. This interpretation is further supported by the intrusive character of the white chert within the dark-colored chert seen at the thin-section scale (Fig. 3) and by the intrusive character of the black chert veins within the stratiform chert seen at the outcrop scale (Fig. 1).

5.3 High-temperature hydrothermal alteration in sample #2.

The ratios R_{D3} and R_{D4} of sample #2, calculated from the hyperspectral map data, are much lower (0.03 and 0.03, respectively) than those calculated for sample #1 (Fig. 7a). These low values are consistent with a higher peak temperature, likely reflecting a different generation of hydrothermal alteration overprint. However, the spectral data from punctual analyses strongly differs from this trend. All but two points in this dataset have R_{D3} and R_{D4} values that fall in the range of the stratiform chert CM. Apparently, by chance some low-ordered CM was analyzed by punctual analysis, which does not reflect the bulk CM. This discrepancy demonstrates the limited use of a few punctual analyses, as they reflect only a limited range in the CM structural variability.

5.4 Tentative geothermometry

As discussed in theory part, the ratios R_{A1}, R_{A2}, and R_2 can only be used tentatively as indicators of peak-temperature. These geothermometers were calibrated with CMs that represent a common precursor and occur in metapelitic metamorphic rocks (Beyssac et al., 2002; Lahfid et al., 2010). The CMs that are studied here do not necessarily represent a common precursor, and occur in cherts. Regional metamorphism and local hydrothermal fluid circulations have resulted in a wide range of peak temperatures of the Apex chert CM through time. As follows from the discussion in paragraph 5.1 this temperature range apparently spans the higher end of the R_{A1} geothermometer and the lower end of the R_2 geothermometer. This implies that the two thermometers based on R_2 and R_{A1} should be used for temperature estimates of samples #1, #2, and samples #4 and #5, respectively. As shown in paragraph 5.2., sample #6 consists of both a stratiform phase and an infiltrating hydrothermal phase. For this sample, the R2-thermometer should be used for the CM in white chert (#6-2) and the RA1-thermometer for the CM in dark gray chert (#6-1). Using equation 2, a tentative temperature of 350°C is obtained for sample #1 and of 360°C for #2 and #6-2. Using equation 4 a tentative temperature of 300°C is obtained for samples #4 and #5 and of ~265°C for #6-1. It is speculated here that these temperatures indeed could represent the peak temperature of hydrothermal fluids and of regional metamorphism, respectively. These ranges of temperatures are in line with temperature estimated from the mineralogical assemblages (van Kranendonk, 2006).

5.5 A disordered pool of Organic Matter in Apex chert

The punctual and the hyperspectral map analyses have shown that there is significant variability in CM structure throughout the Apex chert and the associated hydrothermal chert veins. The lowest degree of structural order is preserved in the stratiform chert (samples #4, #5 and #6-1), and appears to have experienced only greenschist-facies regional metamorphism. The highest degree of structural order is preserved in the cross-cutting chert veins (samples #1 and #2), and represents temperatures that are slightly higher than that of regional metamorphism.

In a R_{D4} vs R_{D3} diagram (Fig. 8a), these different CMs define a linear correlation of slope ~1. In contrast, analyses performed on sample #3 show a random distribution that strongly deviates from this linear trend (Fig. 8a). The spectral data of sample #3 show high FWHM-D/FWHM-G (1.1-2.1) and low I_D/I_G (0.8-1.2) relative to the stratiform chert CM (FWHM-D/FWHM-G =1.2-1.45; I_D/I_G=1.2-1.5) and black chert vein CM (FWHM-D/FWHM-G =1.1-1.3; I_D/I_G=1.35-1.65) (Fig. 8b). This indicates that the CM of sample #3 is less organized than that of the stratiform cherts. The random pattern of sample #3 in the diagram RD3 vs RD4 indicates a lack of correlation between the bands D3 and D4. Importantly, the CM in sample #3 is in close association with randomly distributed hematite of secondary origin. It was shown by Marshall et al. (2011) that one of the Raman bands of hematite (1320 cm^{-1}) is partially overlapping with the D-band of CM. The cloud pattern defined by sample #3 (Fig. 8a) may therefore be an artifact of the Raman-band-fitting protocol. Alternatively, this degree of disorder in the CM of sample #3 is real, and reflects features inherited either from different metamorphic/hydrothermal overprints or from a late stage meteoric alteration.

A similar 'loss of order' due to post-emplacement phenomena could explain the Raman spectra reported by Olcott Marshall et al. (2012). In their study, the primary CM

phase (E1-E2) is concordant with the signature of 'feeder vein chert CM' and the secondary CM phase (E3) is concordant with that of 'stratiform chert CM' when plotted in a I_D/I_G vs FWHM-D/FWHM-G diagram (dotted lines, Fig. 8b). The occurrence of hematite in the sample analyzed by these authors suggests that this CM could have been influenced by different metamorphic/hydrothermal overprints or a late stage contamination during meteoric alteration.

Likewise, the spectrum of the CM in the microfossils described by Schopf et al. (2007) is, to the naked eye, very similar to the spectra of the sample #3 (Fig. 4f). Indeed, the D-band displays the same pointy shape, ID~IG and FWHM-D>1.5FWHM-G. The field where this spectrum is the more likely to fall is the upper range of the diagram (crosshatched zone, Fig. 8b). This suggests that the CM in putative microfossils can represent altered organic matter that bears little information on the original precursor.

7. Conclusions

Many Archean chert deposits have experienced sub-seafloor hydrothermal fluid circulation followed by low-grade regional metamorphism. The CM in such rocks can thus display various degrees of structural ordering. In rocks with a complex thermal history such as the Apex Chert and particularly when peak metamorphism has reached only lower greenschist-facies, it is essential that proper and representative Raman spectral data of each stage of thermal alteration are obtained. We demonstrated here that this depends critically on a precise and complete band decomposition protocol, use of the appropriate ratios, and acquisition of a statistically meaningful set of spectra.

8. Acknowledgments

This work was supported by ANR eLIFE2 to Pascal Philippot. E. Muller is thanked for her help during the Raman spectra acquisition. We thank E. Quirico, H. Busemann and an anonymous reviewer for their constructive remarks that improved the manuscript. This is IPGP contribution #...

9. References

Aoya M., Kouketsu Y., Endo S., Shimizu H., Mizukami T., Nakamura D., and Wallis S. (2010) Extending the applicability of the Raman carbonaceous-material geothermometer using data from contact metamorphic rocks. *Journal of Metamorphic Geology* **28**, 895-914.

Barker C. (1996) Thermal modeling of petrol generation: theory and application. *Developments in petroleum science* **45,** Elsevier.

Behar F., Lorant F. and Lewan M. (2008) Role of NSO compounds during primary cracking of a type II kerogen and a Type III lignite. *Organic Geochemistry* **39**, 1-22.

Bernard S., Beyssac O., Benzerara K., Findling N., Tzvetkov G., and Brown Jr G. E. (2010) XANES, Raman and XRD study of anthracene-based cokes and saccharose-based chars submitted to high-temperature pyrolysis. *Carbon* **48**, 2506-2516.

Beyssac O., Goffé B., Chopin C., and Rouzaud J.-N. (2002) Raman spectra of carbonaceous material in metasediments: a new geothermometer. *Journal of Metamorphic Geology* **20**, 859-871.

Beyssac O., Goffé B., Petitet J.-P., Froigneux E., Moreau M., and Rouzaud J.-N. (2003) On the characterization of disorded and heterogeneous carbonaceous materials by Raman spectroscopy. *Spectrochimica Acta Part A* **59**, 2267-2276.

Bonal L., Quirico E., Bourot-Denise M., and Montagnac G. (2006) Determination of the petrologic type of CV3 chondrites by Raman spectroscopy of included organic matter. *Geochimica et Cosmochimica Acta* **70**, 1849-1863.

Brasier M. D., Green O. R., Jephcoat A. P., Kleppe A. K., van Kranendonk M. J., Lindsay J. F., Steele A., and Grassineau N. V. (2002) Questioning the evidence for Earth's oldest fossils. *Nature* **416**, 76-81.

Brasier M. D., Green O. R., Lindsay J. F., McLoughlin N., Steele A., and Stoakes C. (2005) Critical testing of Earth's oldest putative fossil assemblage from the 3.5 Ga Apex chert, Chinaman Creek, Western Australia. *Precambrian Research* **140**, 55-102.

Brasier M. D., Green O. R., Lindsay J. F., McLoughlin N., Stoakes C. A., Brasier A. T., and Wacey D. (2011). Geology and putative microfossil assemblage of the c. 3460 Ma 'Apex chert', Chinaman creek, Western Australia - A field and petrographic guide. Geological Survey of Western Australia, Record 2011/7, 60p.

Brasier M. D., McLoughlin N., Green O. R. and Wacey D. (2006) A fresh look at the fossil evidence for early Archean cellular life. *Philisophical Transactions of the Royal Society B* **361**, 887-902.

Buseck P. R. and Huang B.-J. (1985) Conversion of carbonaceous material to graphite during metamorphism. *Geochimica et Cosmochimica Acta* **49**, 2003-2016.

Busemann H., Alexander C. M. O. D., and Nittler L. R. (2007) Characterization of insoluble organic matter in primitive meteorites by microRaman spectroscopy. *Meteoritics & Planetary Science* **42**, 1347-1416.

Bustin R. M., Ross J. V., and Rouzaud J.-N. (1995) Mechanisms of graphite formation from kerogen: experimental evidence. *International Journal of Coal Geology* **28**, 1-36.

De Gregorio B. T. and Sharp T. G. (2003) Determining the biogenecity of microfossils in the Apex chert, Western Australia. Thirty-fourth Lunar and Planetary Science conference, Houston, Texas, Abstracts, 1267.

De Gregorio B. T. and Sharp T. G. (2006a) The structure and distribution of carbon in 3.5 Ga Apex chert: implications for the biogenecity of Earth's oldest putative microfossils. *American Mineralogist* **91**, 784-789.

De Gregorio B. T. and Sharp T. G. (2006b) Possible abiotic formation of kerogen-like carbon in the Strelley Pool chert. Thirty-seventh Lunar and Planetary Science conference, Houston, Texas, Abstracts, 2318.

De Gregorio B. T., Sharp T. G., Flynn G. J., Wirick S., and Hervig R. L. (2009) Biogenic origin for Earth's oldest putative microfossils. *Geology* **37**, 631-634.

Dippel B. and Heintzenberg J. (1999) Soot characterization in atmospheric particles from different sources by NIR FT Raman spectroscopy. *Journal of Aerosol Science* **30, Supplement 1**, S907-S908.

Everall N. J., Lumsdon J., and Christopher D. J. (1991) The effect of laser-induced heating upon the vibrational raman spectra of graphites and carbon fibres. *Carbon* **29**, 133-137.

Ferrari A. C. and Robertson J. (2000) Interpretation of Raman spectra spectra of disordered and amorphous carbon. *Physical reviews* **61**, 14095-14107.

Garcia-Ruiz J. M., Hyde S. T., Carnecup A. M., Christy A. G., van Kranendonk M. J., and Welham N. J. (2003) Self-assembled silica-carbonate structures and detection of ancient microfossils. *Science* **302**, 1194-1197.

Jehlicka J. and Bény C. (1992) Application of Raman microspectrometry in the study of structural changes in Precambrian kerogens during regional metamorphism. *Organic Geochemistry* **18**, 211-213.

584 Jehlicka J., Urban O., and Pokorny J. (2003). Raman spectroscopy of carbon and solid
585 bitumens in sedimentary and metamorphic rocks. *Spectrochimica Acta Part A:*
586 *Molecular and Biomolecular Spectroscopy* **59**, 2341-2352.

587 Kagi H., Tsuchida I., Wakatsuki M., Takahashi K., Kamimura N., Iuchi K., and Wada H.
588 (1994) Proper understanding of down-shifted Raman spectra of natural graphite:
589 Direct estimation of laser-induced rise in sample temperature. *Geochimica et*
590 *Cosmochimica Acta* **58**, 3527-3530.

591 Kelemen S.R. and Fang H.L. (2001) Maturity trends in Raman spectra from kerogen and coal.
592 *Energy &Fuels* **15**, 653-658.

593 Lahfid A., Beyssac O., Deville E., Negro F., Chopin C., and Goffé, B. (2010) Evolution of the
594 Raman spectrum of carbonaceous material in low-grade metasediments of the Glarus
595 Alps (Switzerland). *Terra Nova* **22**, 354-360.

596 Larouche N. and Stansfield B. L. (2010) Classifying nanostructured carbons using graphitic
597 indices derived from Raman spectra. *Carbon* **48**, 620-629.

598 Lepland A., van Zuilen M. A., and Philippot, P. (2011) Fluid-deposited graphite and its
599 geobiological implications in early Archean gneiss from Akilia, Greenland.
600 *Geobiology* **9**, 2-9.

601 Lepot K., Williford K.H., Ushikubo T., Sugitani K., Mimura K., Spicuzza M.J., Valley J.W.
602 (2013) Texture-specific isotopic compositions in 3.4 Gyr old organic matter support
603 selective preservation in cell-like structures. *Geochimica et Cosmochimica Acta* **112**,
604 66-86.

605 Lindsay J. F., Brasier M. D., McLoughlin N., Green O. R., Fogel M., Steele A., and
606 Mertzman S. A. (2005) The problem of deep carbone-An Archean paradox.
607 *Precambrian Research* **143**, 1-22.

608 Marshall C. P., Emry J. R., and Olcott Marshall A. (2011) Haematite pseudomicrofossils
609 present in the 3.5-billion-year-old Apex chert. *Nature Geoscience* **4**, 240-243.

610 Marshall C. P., Love G. D., Snape C. E., Hill A. C., Allwood A. C., Walter M. R., Van
611 Kranendonk M. J., Bowden S. A., Sylva S. P., and Summons R. E. (2007) Structural
612 characterization of kerogen in 3.4 Ga Archaean cherts from the Pilbara Craton,
613 Western Australia. *Precambrian Research* **155**, 1-23.

614 Marshall C. P., Mar G. L., Nicoll R. S., and Wilson M. A., (2001) Organic geochemistry of
615 artificially matured conodonts. *Organic Geochemistry* **32**, 1055-1071.

616 Marshall C. P. and Olcott Marshall A. (2011) Hematite and carbonaceous materials in
617 geological samples: A cautionary tale. *Spectrochimica Acta Part A: Molecular and*
618 *Biomolecular Spectroscopy* **80**, 133-137.

619 Mostefaoui S. L., Perron C., Zinner E., and Sagon G. R. (2000) Metal-associated carbon in
620 primitive chondrites: structure, isotopic composition, and origin. *Geochimica et*
621 *Cosmochimica Acta* **64**, 1945-1964.

622 Nasdala L., Brenker F. E., Glinnemann J., Hofmeister W., Gasparik T., Harris J. W., Stachel
623 T., and Reese I. (2003) Spectroscopic 2D-tomography: Residual pressure and strain
624 around mineral inclusions in diamonds. *European Journal of Mineralogy* **15**, 931-935.

625 Nemanich R. J. and Solin S. A. (1979) First- and second-order Raman scattering from finite-
626 size crystals of graphite. *Physical Review B* **20**, 392-401.

627 Nijman W., de Bruijne K. (C.) H., Valkering M.E. (1998) Growth fault control of Early
628 Archaean cherts, barite mounds and chert-barite veins, North Pole Dome, Eastern
629 Pilbara, Western Australia. Precambrian Research **88**, 25-52.

630 Olcott Marshall A., Emry J. R., and Marshall C. P. (2012) Multiple generations of carbon in
631 the Apex chert and Implications for preservation of microfossils. *Astrobiology* **12**,
632 160-166.

633 Olcott Marshall A., Jehlicka J., Rouzaud J.-N., and Marshall C. P. (2013) Multiple
634 generations of carbonaceous material deposited in Apex chert by basin-scale pervasive
635 fluid flow. *Gondwana Research* In press.

636 Olcott Marshall A. and Marshall C. P. (2013) Comment on "Biogenicity of Earth's earliest
637 fossils: A resolution of the controversy" by J. W. Schopf and A. B. Kudryavtsev,
638 Gondwana Research, Volume 22, Issue 3–4, Pages 761–771. *Gondwana Research* **23**,
639 1654-1655.

640 Pasteris J. D. (1989) In situ analysis in geological thinsections by laser Raman microprobe
641 spectroscopy: a cautionary note. *Applied Spectroscopy* **43**, 567-570.

642 Pinti D. L., Hashizume K., Sugihara A., Massault M., and Philippot P. (2009) Isotopic
643 fractionation of nitrogen and carbon in Paleoarchean cherts from Pilbara Craton,
644 Western Australia: Origin of 15N-depleted nitrogen. *Geochimica et Cosmochimica*
645 *Acta* **73**, 3819-3848.

646 Pinti D. L., Mineau R., and Clement V. (2013) Comment on "Biogenicity of Earth's earliest
647 fossils: a resolution of the controversy" by J. William Schopf and Anatoliy B.
648 Kudryavtsev, Gondwana Research 22 (2012), 761–771. *Gondwana Research* **23**,
649 1652-1653.

650 Qu Y., van Zuilen M. A., and Lepland A. (2011) Raman spectroscopic analysis of
651 heterogeneous carbonaceous matter in the 2.0 Ga Zaonega Fm, Karelia, Russia.
652 Goldschmidt Geochemistry Conference, Prague, Czech Republic.

653 Qu Y., Črne A. E., Lepland A., and van Zuilen M. A. (2012) Methanotrophy in a
654 Paleoproterozoic oil field ecosystem, Zaonega Formation, Karelia, Russia. *Geobiology*
655 **10**, 467-478.

656 Qu Y., van Zuilen M. A., Lepland A, Črne A. E., Fliegel D., Somelar P. (2013) Structural
657 variation of metamorphosed carbonaceous material in the 2.0 Ga Zaonega Formation,
658 Karelia, Russia. *Precambrian Research*, In Review.

659 Quirico E., Raynal P.-I., and Bourot-Denise M. (2003) Metamorphic grade of organic matter
660 in six unequilibrated ordinary chondrites. *Meteoritics & Planetary Science* **38**, 795-
661 811.

Rahl J. M., Anderson K. M., Brandon M. T. and Fassoulas C. (2005) Raman spectroscopic carbonaceous material thermometry of low-grade metamorphic rocks: Calibration and application to tectonic exhumation in Crette, Greece. *Earth and Planetary Science Letters* **240**, 339-354.

Ross J. V. and Bustin R. M. (1990) The role of strain energy in creep graphitization of anthracite. *Nature* **343**, 58-60.

Sadezsky A., Muckenhuber H., Grothe H., Niessner R., and Pöschl U. (2005) Raman microspectroscopy of soot and related carbonaceous materials: Spectral analysis and structural information. *Carbon* **43**, 1731-1742.

Schopf J. W. (1993) Microfossils of the Early Archean Apex chert: New evidence of the antiquity of life. . *Science* **260**, 640-646.

Schopf J. W. and Kudryavtsev A. B. (2012) Biogenicity of Earth's earliest fossils: A resolution of the controversy. *Gondwana Research* **22**, 761-771.

Schopf J. W. and Kudryavtsev A. B. (2013) Reply to the comments of D.L. Pinti, R. Mineau and V. Clement, and of A.O. Marshall and C.P. Marshall on "Biogenicity of Earth's earliest fossils: A resolution of the controversy" by J. William Schopf and Anatoliy B. Kudryavtsev, Gondwana Research 22 (2012), 761-771. *Gondwana Research* **23**, 1656-1658.

Schopf J. W., Kudryavtsev A. B., Agresti D. G., Wdowiak T. J., and Czaja A. D. (2002). Laser-Raman imagery of Earth's earliest fossils. *Nature* **416**, 73-76.

Schopf J. W., Kudryavtsev A. K., Czaja A. C., and Tripathi A. B. (2007) Evidence of Archean Life: Stromatolites and microfossils. *Precambrian Research* **158**, 141-155.

Schopf J. W. and Packer B. M. (1987) Early Archean (3.3-Billion to 3.5-Billion-Year-Old) Microfossils from Warrawoona Group, Australia. *Science* **237**, 70-73.

Thébaud N. and Rey P. F. (2013) Archean gravity-driven tectonics on hot and flooded continents: Controls on long-lived mineralised hydrothermal systems away from continental margins. *Precambrian Research* **229**, 93-104.

Tice M., Bostick B. C., and Lowe D. R. (2004) Thermal history of the 3.5-3.2 Ga Onverwacht and Fig Tree Groups, Barberton greenstone belt, South Africa, inferred by Raman microspectroscopy of carbonaceous material. *Geology* **32**, 37-40.

Tuinstra F. and Koenig J. L. (1970) Raman spectrum of graphite. *Journal of Chemical Physics* **53**, 1126-1130.

Ueno Y., Yoshioka H., Maruyama S., and Isozaki Y. (2004) Carbon isotopes and petrography of kerogens in 3.5-Ga hydrothermal silica dikes in the North Pole area, Western Australia. *Geochimica et Cosmochimica Acta* **68**, 573-589.

van den Boorn S. H. J. M., van Bergen M. J., Nijman W., and Vroon P. Z. (2007) Dual role of seawater and hydrothermal fluids in Early Archean chert formation: evidence from silicon isotopes. *Geology* **35**, 939-942.

van Kranendonk M. J. (2000) Geology of the North Shaw 1:100 000 sheet: Western Australia Geological Survey, 1:100 000. Geological Series Explanatory Notes, 86 p.

van Kranendonk M. J. (2006) Volcanic degassing, hydrothermal circulation and the flourishing of early life on Earth: a review of the evidence from c. 3490-3240 Ma rocks of the Pilbara supergroup, Pilbara craton, western Australia. *Earth-Science Reviews* **74**, 197-240.

van Kranendonk M. J., Hickman A. H., Smithies R. H., and Nelson D. R. (2002) Geology and tectonic evolution of the Archean North Pilbara Terrain, Pilbara craton, western Australia. *Economic Geology* **97**, 695-732.

van Kranendonk M. J. and Pirajno F. (2004) Geochemistry of metabasalts and hydrothermal alteration zones associated with c. 3.45 Ga chert and barite deposits: implications for the geological setting of the Warrawoona Group, Pilbara craton, Australia. *Geochemistry: Exploration, Environment, Analysis* **4**, 253-278.

van Zuilen M.A., Fliegel D., Wirth R., Lepland A., Qu Y., Schreiber A., Romashkin A. E., and Philippot P. (2012) Mineral-templated growth of natural graphite films. *Geochimica et Cosmochimica Acta* **83**, 252-262.

Wacey D., Saunders M., Brasier M.D., Kilburn, M.R. (2011) Earliest microbially mediated pyrite oxidation in ~3.4 billion-year-old sediments. *Earth and Planetary Science Letter* **301**, 393-402.

Wang A., Dhamenincourt P., Dubessy J., Guerard D., Landais P., and Lelaurain M. (1989) Characterization of graphite alteration in an uranium deposit by micro-Raman spectroscopy, X-ray diffraction, transmission electron microscopy and scanning electron microscopy. *Carbon* **27**, 209-218.

Waples D.W. (1994) Maturity modeling: thermal indicators, hydrocarbon generation, and oil cracking. In *The petroleum system – from source to trap (eds. L.B. Magoon and W.G. Dow) , AAPG Memoir* **60**, 285-306

Wopenka B. and Pasteris J. D. (1991) Raman spectra of graphite as indicators of degree of metamorphism. *Canadian Mineralogist* **29**, 1-9.

Wopenka B. and Pasteris J. D. (1993) Structural characterization of kerogens to granulite-facies graphite: Applicability of Raman microprobe spectroscopy. *American Mineralogist* **78**, 533-557.

Figure captions

734 **Figure 1:** Simplified geological maps of a) the North Pilbara Craton (modified from Thébaud
735 and Rey, 2013) and of b) the Apex chert (modified from Brasier et al., 2005). The numbers
736 correspond to the location of the samples analyzed in this study (see Fig. 3).

737

738 **Figure 2**: Decomposition of the Raman spectrum of disordered CM. a) Disorder-associated
739 bands D2, D3 and D4 are distinguished as well as the main D1 and G bands (see Sadezky et
740 al. (2005) for band labeling and fitting intervals). Each of the five fitted bands has a Gaussian-
741 Lorentzian shape where the percentage of Gaussian can vary freely. The band position are
742 fixed between 1340-1360 cm^{-1} for D1, 1615-1625cm^{-1} for D2, 1490-1510 cm^{-1} for D3, 1150-
743 1250cm^{-1} for D4 and 1580-1610cm^{-1} for G. The intensity of D2 was limited to less than half
744 of that of the G-band. For the D4-band, the maximum band width (FWHM) was limited at a
745 maximum of 200 cm^{-1}. This constraint was necessary to prevent the generation of
746 unreasonably large D4-bands in some of the spectra. b) Following protocol 2, only the main
747 bands of D and G were distinguished. The band positions are fixed between 1340-1360 cm^{-1}
748 for D and 1580-1610 cm^{-1} for G.

749

750 **Figure 3**: Thin sections of all samples analyzed in this study. White dots represent Raman
751 spectral analyses of carbonaceous matter in stratiform chert. Black dots represent
752 carbonaceous matter in intrusive black cherts zones. Squares correspond to locality where
753 Raman maps were acquired. Sample #1 maps are located in the same area, while the maps #6-
754 1 and #6-2 are located in the dark gray chert and in the white chert, respectively.

755

Figure 4: Representative spectra for the 6 samples obtained by punctual analyses showing first and second order bands.

Figure 5: Example of apparent ambiguity in the use of the ratios R2 and RA1 for punctual analysis in samples #1, #4 and #5. a) I_D/I_G vs R_2 ratios. R_2 and I_D/I_G ratios are lower for the stratiform chert CMs (white dots and diamonds) than for the black chert veins CMs (black dots) indicating that the CM order is higher for the stratiform cherts than for the feeder black chert veins. b) I_D/I_G vs R_{A1} ratios. R_{A1} and I_D/I_G are lower for the stratiform cherts than for the feeder black chert veins indicating that the CM order is higher for the hydrothermal cherts than for the stratiform cherts. Filled and unfilled grey points correspond to the mean of the analyses for sample #1 and samples #4-5, respectively. Error bars correspond to 1 standard deviation.

Figure 6: Two pools of CM in the Apex chert. a) Mean spectrum for stratiform chert CM normalized to D1. I_{D3} and I_{D4} are relatively intense corresponding to a poorly organized CM, which argues for a low peak. b) Mean spectrum for black chert veins normalized to D1. I_{D3} and I_{D4} are relatively low, which correspond to a better organized CM and thus to a higher peak temperature. c) R_{D4} vs R_{D3} for samples #1, #4 and #5. Two well separated groups of CM can be recognized; black chert vein CM with low R_{D3} and R_{D4} and stratiform chert CM with high R_{D3} and R_{D4}. Filled and unfilled grey points correspond to the mean of the analyses for sample #1 and samples #4-5, respectively. Error bars correspond to 1 standard deviation. d) R_{D4} vs R_{D3} for all samples. Samples #2 and #6 have a 'stratiform chert signature' which is contrary to what is expected. Sample #3 shows a low-ordered CM.

779

780 **Figure 7:** Distribution of the CM in the stratiform chert and the black chert veins showed by
781 a) histograms of R_{D3} ratios for samples #1 (white), #2 (light gray), #4 and #5 (black). b)
782 Histogram of R_{D3} ratios for sample #6; light gray histogram is for the intrusive white chert
783 and the dark gray histogram is for the darker chert. The white chert CMs fall within the range
784 of black chert veins CMs whereas the darker chert CMs fall within the range of the stratiform
785 chert CMs.

786

787 **Figure 8** Poorly ordered CM in the Apex chert, showed in a) R_{D3} vs R_{D4} diagram. All samples
788 align themselves on a slope with a coefficient of ~1 except for measurements of sample #3
789 suggesting post-emplacement phenomena b) FWHM-D/FWHM-G vs I_D/I_G. The data for
790 sample #3 have high FWHM-D/FWHM-G and low I_D/I_G relative to the feeder veins and
791 stratiform cherts, which indicate poorly organized CM with a metamorphic temperature lower
792 than regional metamorphism and hydrothermal alteration. The range where the spectrum of
793 Apex chert showed in Schopf et al. (2007) is represented with crosshatches. It coincides with
794 the post-emplacement altered CM range. The mean ID/IG ratio calculated by Olcott Marshall
795 et al. (2012) for the two identified groups is shown with dashed lines. Primary phase (E1) has
796 feeder vein chert signature (hydrothermal origin) and their secondary phase has a stratiform
797 chert signature (regional metamorphism) linked with high hematite content. Their secondary
798 phase could arise from the oxidation of the hydrothermally-derived chert during weathering.

799

800 **Figure S1:** Representative spectra for the 6 samples obtained with hyperspectral mapping
801 analysis.

Table 1: Comparison between ratios calculated for embedded CM and CM at the sample surface.

Table 2: Mean values calculated for the different ratio from the punctual analysis and the map analysis. I_D/I_G, A_D/A_G are calculated with the protocol 2. R_2, R_{A1}, R_{A2}, R_{D3} and R_{D4}, T_{R2}, T_{RA1} and T_{RA2} are calculated with protocol 1. The tentative temperatures that must be considered are in bold case. Positions of D (ω-D1) and G (ω-G), FWHM-D and FWHM-G and the ratio FWHM-D/FWHM-G are calculated from protocol 1 (*) and from protocol 2 (**). Errors correspond to 2 standard deviations.

Table ST1: Characteristics of the hyperspectral maps for each sample

Table ST2: Values calculated for the different ratio from the punctual analysis for each punctual analysis. I_D/I_G, A_D/A_G are calculated with the protocol 2. R_2, R_{A1}, R_{A2}, R_{D3} and R_{D4}, T_{R2}, T_{RA1} and T_{RA2} are calculated with protocol 1. The tentative temperatures that must be considered are in bold case. Positions of D (ω-D1) and G (ω-G), FWHM-D and FWHM-G and the ratio FWHM-D/FWHM-G are calculated from protocol 1 (*) and from protocol 2 (**). Errors correspond to 2 standard deviations.

822 **Table ST3:** Values calculated for the different ratio from the map analysis for each individual
823 spectrum. I_D/I_G, A_D/A_G are calculated with the protocol 2. R_2, R_{A1}, R_{A2}, R_{D3} and R_{D4}, T_{R2},
824 T_{RA1} and T_{RA2} are calculated with protocol 1. The tentative temperatures that must be
825 considered are in bold case. Positions of D (ω-D1) and G (ω-G), FWHM-D and FWHM-G
826 and the ratio FWHM-D/FWHM-G are calculated from protocol 1 (*) and from protocol 2
827 (**). Errors correspond to 2 standard deviations.

Figure 1

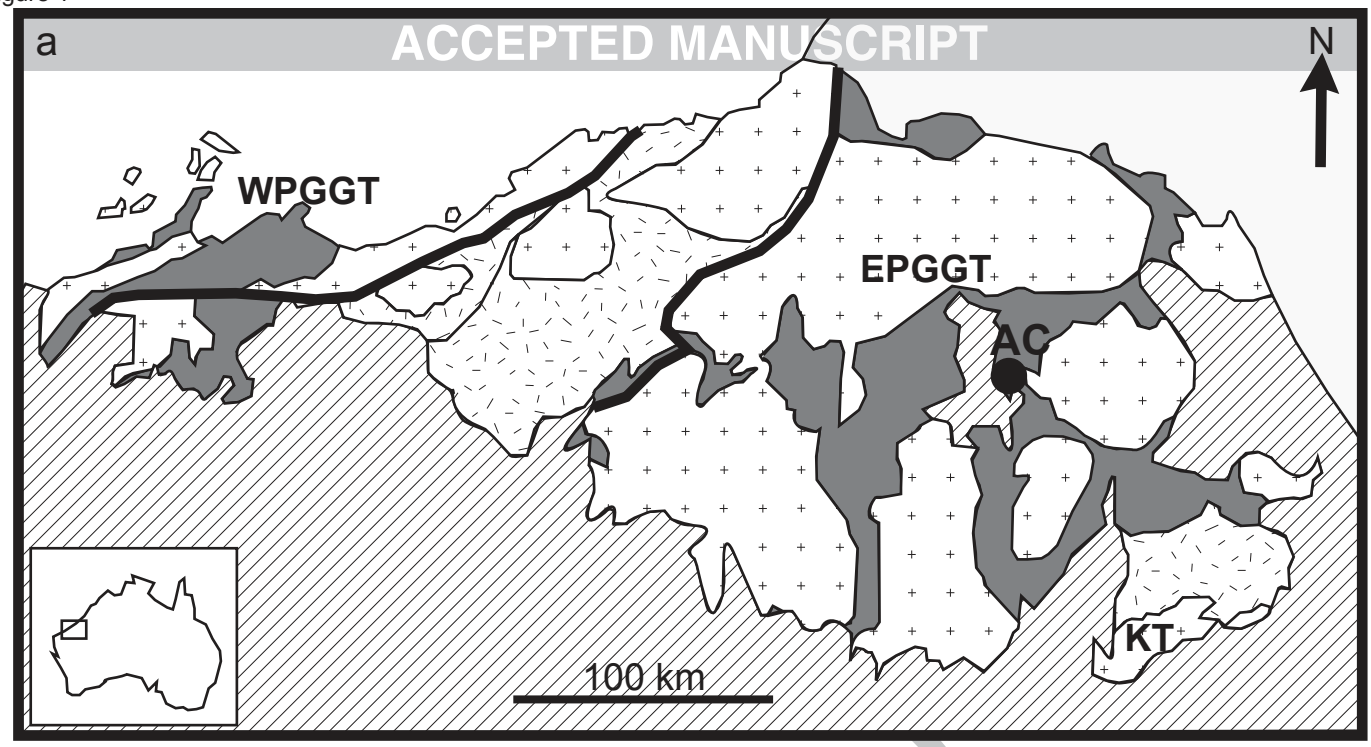

Greenstone
Sedimentary Basins
Phenerozoic cover
Gratinoid complex
Hamersley Basin
KT: Kurrana Terrane
AC: Apex Chert

WPGGT: West Pilbara Granite-Greenstone Terrane
EPGGT: East Pilbara Granite-Greenstone Terrane

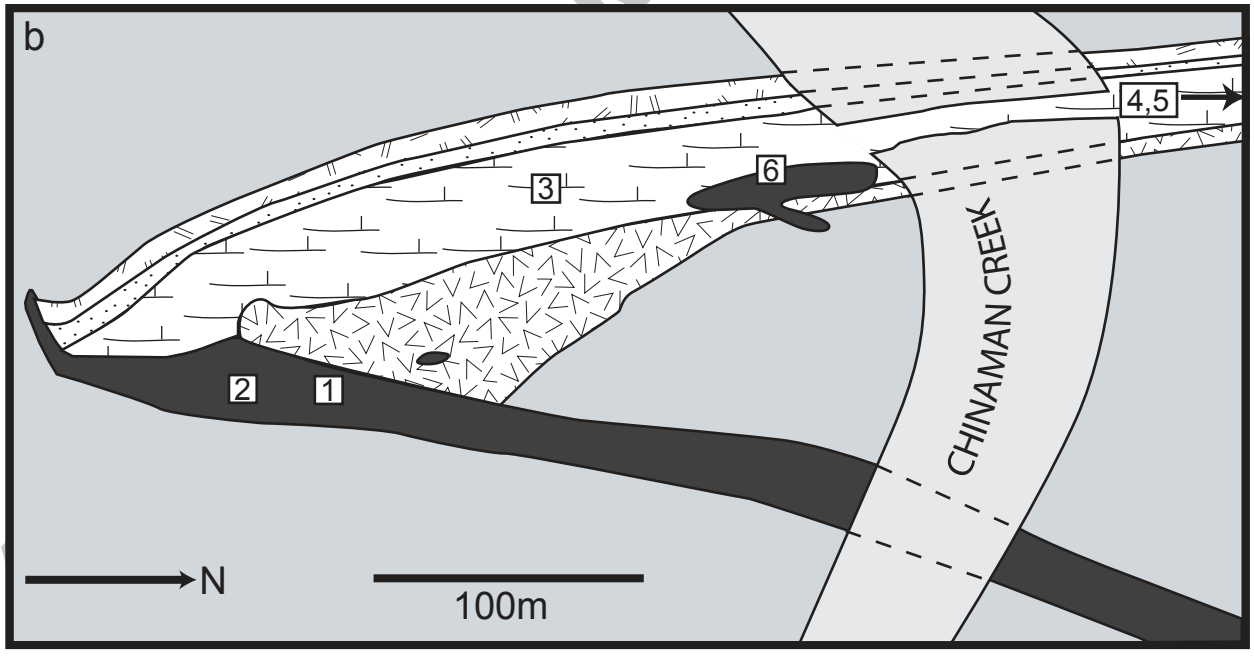

Pillow basalt and komatiite
Pyroclastic breccia
Gray-green glassy tuff
Green tuff
Stratiform chert
Intruding or dilatational black chert

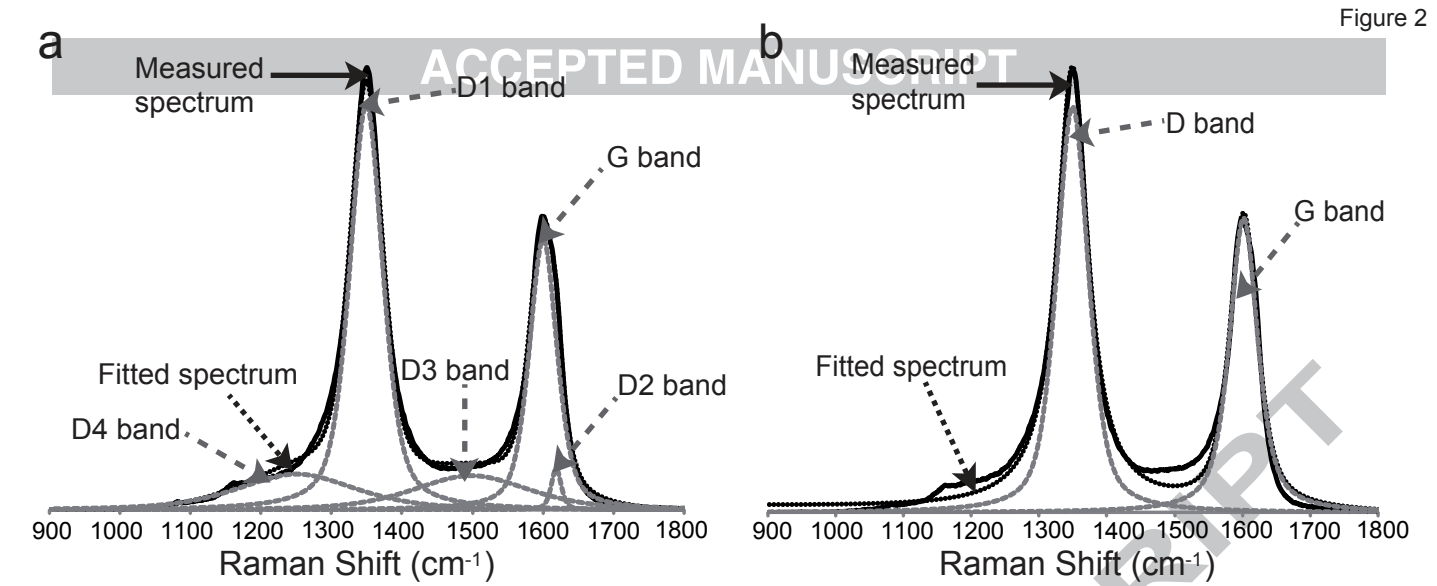

Figure 3

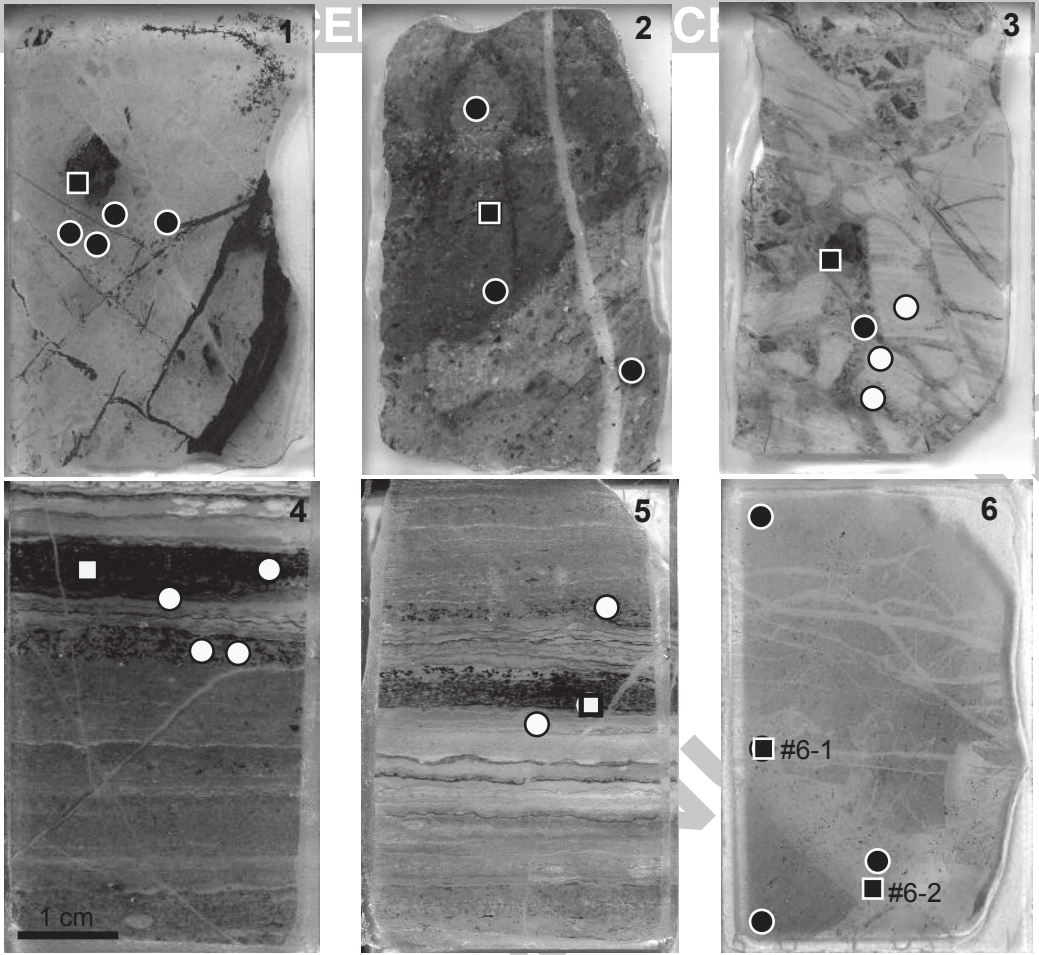

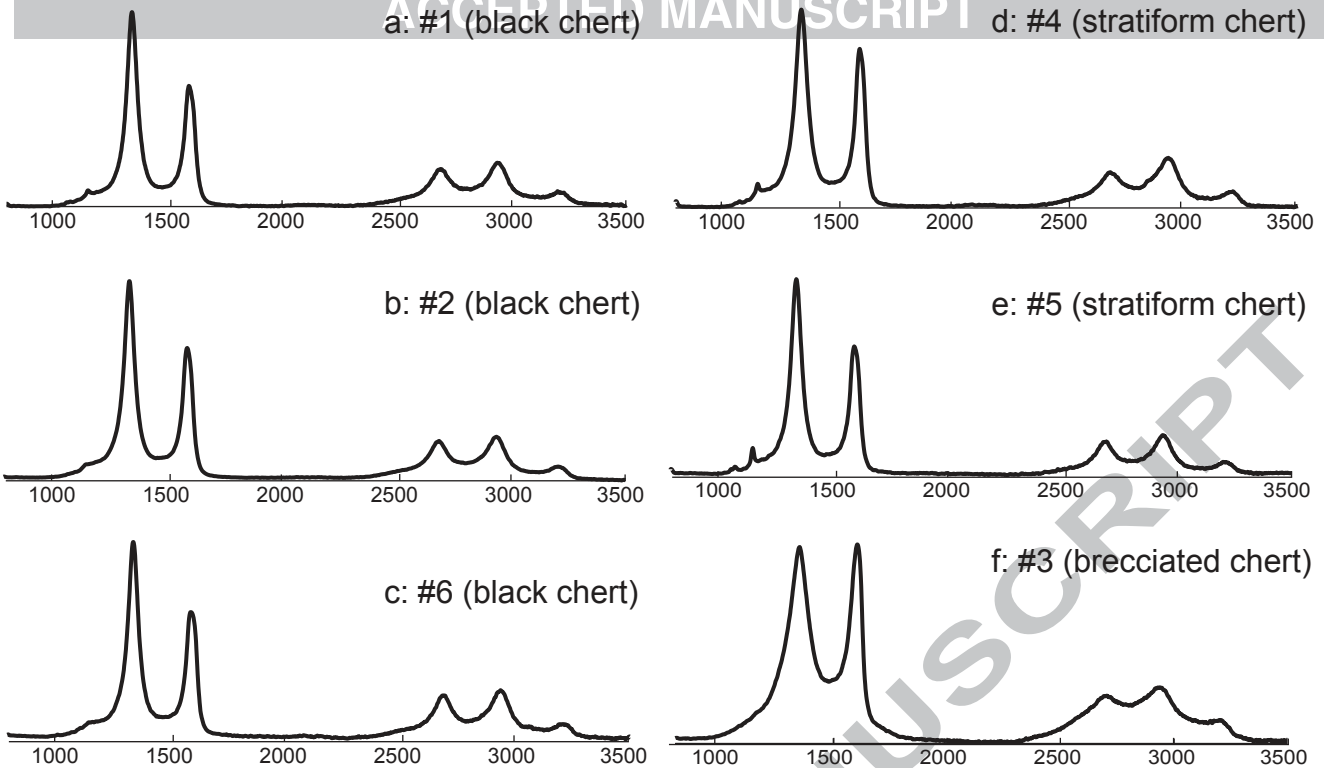

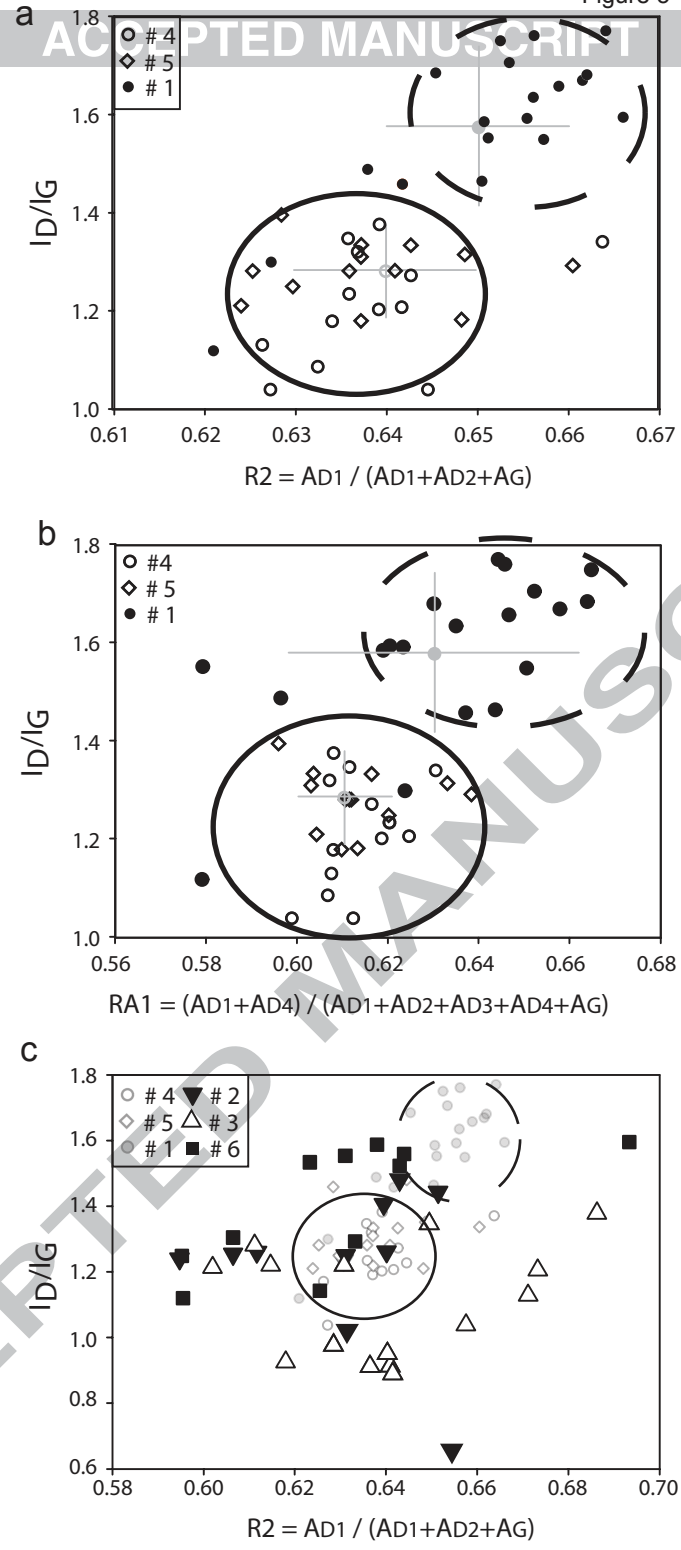

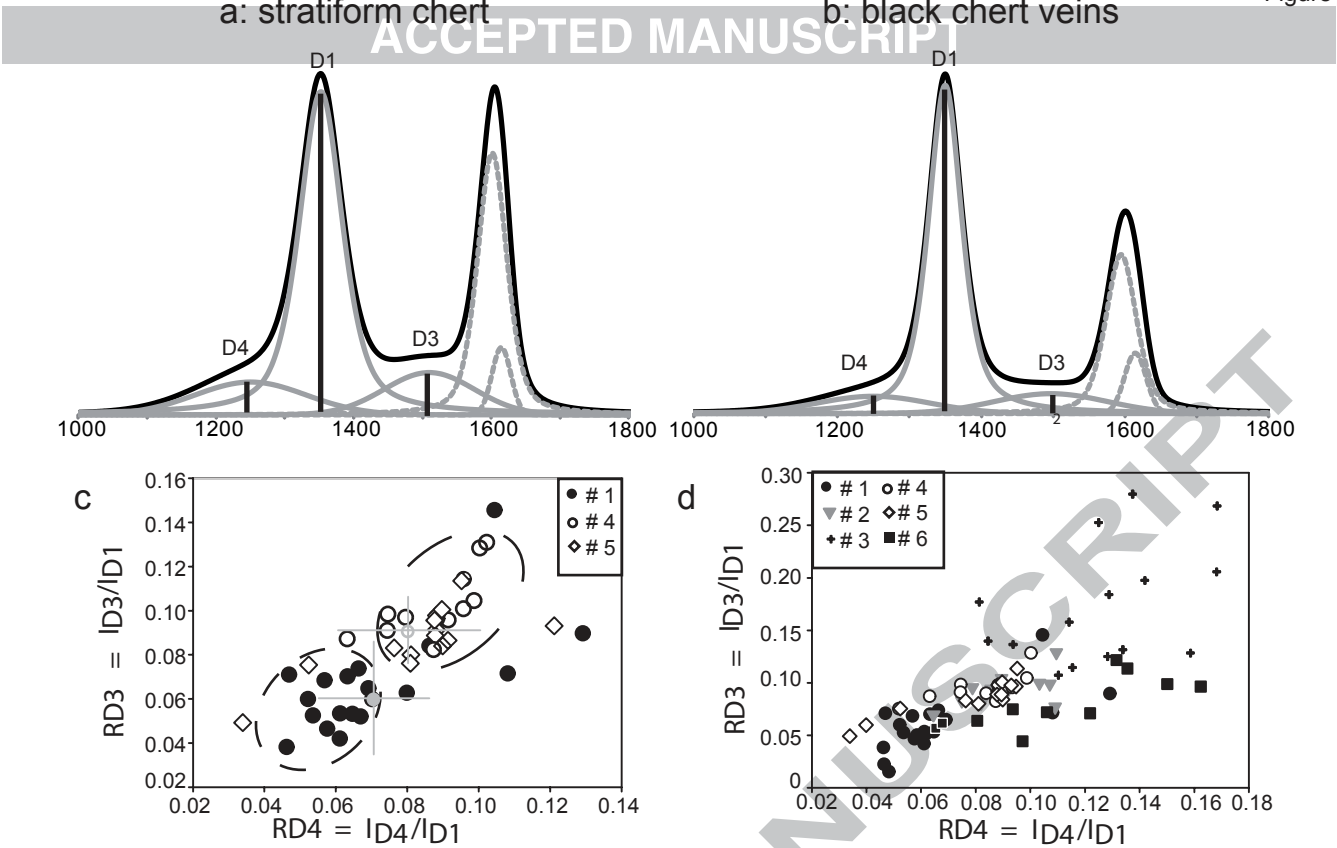

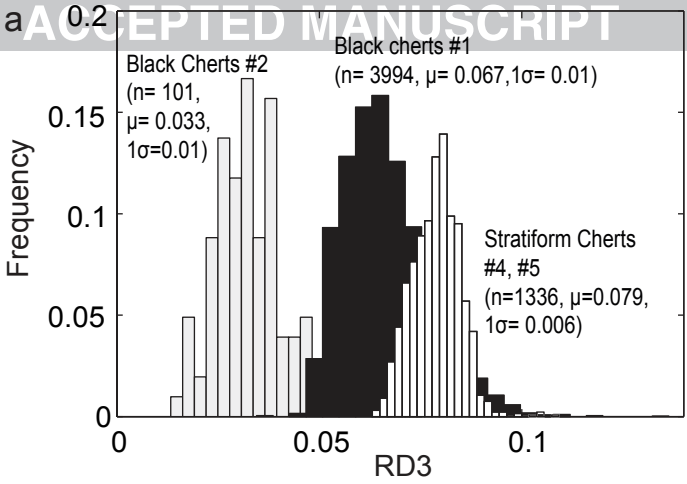

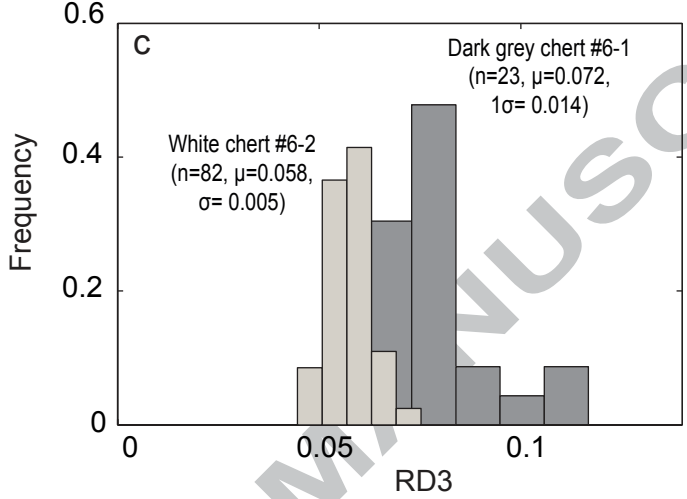

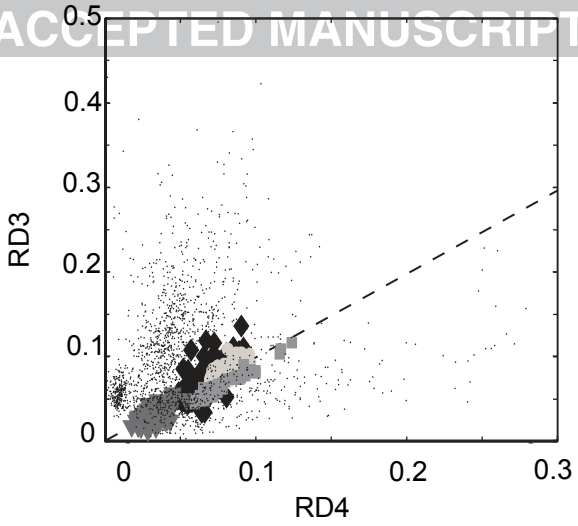

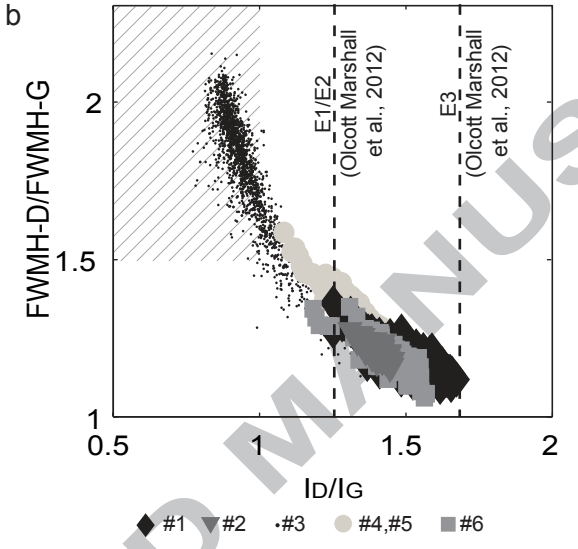

	Type	D1-w	R2	RA1	RA2	ID/IG	AD/AG	RD3	RD4	Type	D1-w	R2	RA1	RA2	ID/IG	AD/AG	RD3	RD4
1	*Embedded*	53.54	0.66	0.65	1.82	1.76	1.92	0.05	0.06	*Surface*	53.67	0.66	0.64	1.80	1.75	1.92	0.05	0.07
1	*Embedded*	54.25	0.66	0.66	1.92	1.67	1.90	0.05	0.07	*Surface*	60.60	0.63	0.61	1.57	1.45	1.78	0.08	0.09
1	*Embedded*	56.94	0.66	0.65	1.86	1.55	1.91	0.04	0.05	*Surface*	56.96	0.65	0.64	1.79	1.54	1.88	0.06	0.07
1	*Embedded*	53.14	0.65	0.65	1.88	1.71	1.90	0.08	0.09	*Surface*	54.80	0.64	0.63	1.68	1.62	1.84	0.06	0.08
1	*Embedded*	53.02	0.65	0.66	1.98	1.68	1.85	0.05	0.06	*Surface*	53.10	0.65	0.64	1.80	1.72	1.88	0.04	0.06
1	*Embedded*	52.32	0.65	0.66	1.98	1.75	1.90	0.06	0.07	*Surface*	56.83	0.65	0.64	1.80	1.55	1.84	0.06	0.07
1	*Embedded*	54.13	0.66	0.65	1.83	1.66	1.90	0.04	0.06	*Surface*	53.58	0.66	0.65	1.84	1.71	1.87	0.04	0.05
1	*Embedded*	57.68	0.64	0.64	1.76	1.46	1.78	0.06	0.08	*Surface*	60.51	0.63	0.63	1.68	1.39	1.73	0.06	0.07
1	***Mean***	***54.38***	***0.65***	***0.65***	***1.88***	***1.65***	***1.88***	***0.05***	***0.07***	***Mean***	***56.26***	***0.65***	***0.64***	***1.75***	***1.59***	***1.84***	***0.06***	***0.07***
1	***2σ***	***3.84***	***0.01***	***0.02***	***0.16***	***0.21***	***0.09***	***0.03***	***0.03***	***2 σ***	***6.04***	***0.02***	***0.03***	***0.18***	***0.27***	***0.12***	***0.03***	***0.02***
4	*Embedded*	61.35	0.64	0.61	1.57	1.35	1.84	0.08	0.09	*Surface*	63.73	0.61	0.56	1.29	1.37	1.62	0.13	0.10
4	*Embedded*	68.01	0.64	0.62	1.62	1.20	1.80	0.13	0.10	*Surface*	65.20	0.64	0.62	1.60	1.32	1.83	0.10	0.09
4	*Embedded*	67.28	0.64	0.62	1.66	1.21	1.79	0.10	0.10	*Surface*	68.16	0.64	0.62	1.64	1.19	1.80	0.10	0.10
4	*Embedded*	63.88	0.64	0.61	1.55	1.32	1.82	0.10	0.09	*Surface*	61.51	0.64	0.62	1.63	1.34	1.82	0.09	0.09
4	*Embedded*	66.33	0.64	0.62	1.63	1.23	1.77	0.10	0.09	*Surface*	68.19	0.64	0.62	1.60	1.20	1.79	0.10	0.10
4	*Embedded*	66.13	0.64	0.62	1.61	1.27	1.81	0.10	0.10	*Surface*	68.67	0.64	0.62	1.62	1.19	1.82	0.11	0.10
4	***Mean***	***65.50***	***0.64***	***0.62***	***1.61***	***1.26***	***1.81***	***0.09***	***0.08***	***Mean***	***65.91***	***0.64***	***0.61***	***1.56***	***1.27***	***1.78***	***0.09***	***0.08***
4	***2σ***	***4.93***	***0.01***	***0.01***	***0.09***	***0.12***	***0.05***	***0.06***	***0.05***	***2 σ***	***5.83***	***0.03***	***0.04***	***0.27***	***0.16***	***0.16***	***0.07***	***0.06***
5	*Embedded*	64.35	0.63	0.62	1.63	1.25	1.73	0.08	0.09	*Surface*	66.85	0.61	0.60	1.49	1.20	1.77	0.09	0.12
5	*Embedded*	66.13	0.64	0.62	1.61	1.33	1.68	0.09	0.12	*Surface*	58.67	0.64	0.62	1.60	1.37	1.81	0.08	0.08
5	*Embedded*	63.61	0.62	0.60	1.53	1.21	1.72	0.10	0.09	*Surface*	61.78	0.64	0.62	1.63	1.30	1.80	0.09	0.09
5	*Embedded*	66.66	0.64	0.61	1.57	1.28	1.86	0.08	0.08	*Surface*	66.57	0.64	0.62	1.63	1.27	1.80	0.10	0.09
5	*Embedded*	60.69	0.64	0.61	1.57	1.28	1.69	0.09	0.09	*Surface*	64.67	0.63	0.62	1.63	1.19	1.78	0.09	0.10
5	*Embedded*	63.33	0.63	0.61	1.58	1.28	1.69	0.09	0.09	*Surface*	64.71	0.64	0.62	1.61	1.28	1.80	0.10	0.09
5	*Embedded*	63.09	0.64	0.60	1.52	1.33	1.81	0.10	0.09	*Surface*	62.35	0.64	0.61	1.57	1.34	1.80	0.09	0.09
5	*Embedded*	64.69	0.64	0.60	1.52	1.31	1.81	0.10	0.09	*Surface*	62.59	0.64	0.62	1.62	1.24	1.80	0.09	0.09
5	***Mean***	***64.07***	***0.63***	***0.61***	***1.57***	***1.29***	***1.75***	***0.09***	***0.09***	***Mean***	***63.52***	***0.64***	***0.61***	***1.60***	***1.27***	***1.79***	***0.09***	***0.09***
5	***2σ***	***3.74***	***0.01***	***0.01***	***0.08***	***0.08***	***0.13***	***0.02***	***0.02***	***2 σ***	***5.45***	***0.02***	***0.01***	***0.10***	***0.13***	***0.03***	***0.01***	***0.02***

Table. 1

Sample	Type	n	ω-D1*	ω-G*	ω-D1**	ω-G**	FWHM-D1*	FWHM-G*	FWHM-D1/ FWHM-G**	FWHM-D1**	FWHM-G**	FWHM-D1/ FWHM-G**
1	Punctual	19	1350.0 ± 1.3	1597.2 ± 2.0	1349.6 ± 1.5	1600.0 ± 0.9	56.80 ± 10.56	48.58 ± 4.17	1.05 ± 0.36	57.88 ± 12.70	50.88 ± 5.12	1.14 ± 0.20
	Map	*3994*	*1349.9 ± 0.7*	*1596.5 ± 1.2*	*1349.6 ± 0.7*	*1600.2 ± 0.5*	*57.3 ± 3.61*	*48.12 ± 2.04*	*1.19 ± 0.05*	*59.75* ± 5.5	*50.44 ± 2.29*	*1.18 ± 0.06*
2	Punctual	11	1349.4 ± 2.4	1599.1 ± 2.9	1349.1 ± 3.4	1602.4 ± 1.8	62.07 ±13.0	48.38 ± 4.1	1.28 ± 0.35	61.54 ± 15.90	50.02 ± 5.13	1.23 ± 0.4
	Map	*101*	*1348.7 ± 0.5*	*1600.4 ± 1.3*	*1348.5 ± 0.5*	*1602.3 ± 0.4*	*56.84 ± 2.03*	*46.24 ± 1.72*	*1.19 ± 0.05*	*55.41* ± 1.95	*45.72* ± 1.38	*1.21 ± 0.05*
6	Punctual	15	1348.3 ± 3.0	1597.4 ± 4.5	1347.2 ± 3.4	1600.9 ± 2.4	61.56 ± 18.18	47.48 ± 2.48	1.09 ± 0.69	67.33 ± 24.78	52.65 ± 7.38	1.27 ± 0.31
	Map 6-1	*23*	*1347.9 ± 2.2*	*1595.5 ± 2.1*	*1347.5± 2.5*	*1599.3 ± 2.4*	*57.50± 7.17*	*47.70 ± 2.19*	*1.21 ± 0.15*	*60.00 ± 9.64*	*50.77 ± 2.67*	*1.18 ± 0.17*
	Map 6-2	*82*	*1349.5 ± 0.4*	*1598.1 ± 0.9*	*1349.1 ± 0.5*	*1602.0 ± 0.5*	*56.81± 3.13*	*47.73 ± 1.11*	*1.19 ± 0.06*	*58.67± 4.22*	*48.26 ± 1.10*	*1.22 ± 0.08*
4	Punctual	13	1349.7 ± 2.5	1599.4 ± 2.1	1349.1 ± 2.8	1602.6 ± 2.1	66.17 ±6.87	48.72 ± 3.54	1.03± 0.65	69.26 ± 8.83	49.64 ± 1.96	1.40 ± 0.18
	Map	*1225*	*1350.7 ± 0.7*	*1598.9 ± 1.2*	*1350.3 ± 0.8*	*1603.2± 0.7*	*61.18* ± 4.3	*49.15 ± 1.97*	*1.24 ± 0.09*	*64.08* ± 4.78	*49.29* ± 1.58	*1.30 ± 0.09*
5	Punctual	14	1348.9 ± 1.3	1599.1 ± 2.4	1348.5 ± 1.7	1602.1 ±1.4	63.78 ±5 .78	47.74 ± 2.27	0.98 ± 0.60	64.53 ± 8.73	49.14 ± 2.08	1.31 ± 0.17
	Map	*111*	*1349.6 ± 0.4*	*1599.0 ± 0.7*	*1349.0 ± 0.5*	*1602.8 ± 0.5*	*63.26* ± 1.90	*47.05 ± 1.54*	*1.34 ± 0.06*	*66.67 ± 2.39*	*47.94 ± 1.31*	*1.39 ± 0.06*
3	Punctual	15	1350.6 ± 3.9	1599.8± 3.5	1349.8 ±5.5	1601.9 ±2.4	91.82 ±40.68	55.68±8.89	1.40 ± 1.0	106.56± 53.02	60.56 ± 5.63	1.75 ± 0.78
	Map	*1758*	*1350.2± 3.7*	*1598.1 ± 4.5*	*1349.0± 2.4*	*1603.0 ± 2.9*	*94.95 ± 22.88*	*57.40 ± 12.34*	*1.72± 5.03*	*96.02± 22.19*	*53.38± 7.38*	*1.80 ± 0.37*

Sample	Type	n	ID/IG	AD/AG	R2	RA1	RA2	RD3	RD4	TR2	TRA1	TRA2
1	Punctual	19	1.58 ± 0.33	1.89 ± 0.13	0.65 ± 0.02	0.63 ± 0.05	1.73 ± 0.36	0.06 ± 0.05	0.07 ± 0.04	**351.3 ± 10.6**	320.6 ± 63.2	324.7± 79.5
	Map	*3994*	*1.51 ± 0.13*	*1.81 ± 0.08*	*0.64 ± 0.01*	*0.62 ± 0.03*	*1.61 ± 0.18*	*0.07 ± 0.02*	*0.07 ± 0.01*	***349.3 ± 5.8***	*300.5 ± 33.2*	*297.5 ± 39.6*
2	Punctual	11	1.23 ± 0.45	1.66 ± 0.83	0.63 ± 0.04	0.60 ± 0.06	1.51 ± 0.35	0.09 ± 0.03	0.09 ± 0.03	**360.5 ± 16.8**	279.7 ± 75.0	275.4 ± 78.5
	Map	*101*	*1.4 ± 0.06*	*1.71 ± 0.05*	*0.63 ± 0.02*	*0.63± 0.02*	*1.67 ± 0.14*	*0.03 ± 0.02*	*0.03 ± 0.01*	***359.0 ± 3.5***	*312.2 ± 24.8*	*311.5 ± 30.1*
6	Punctual	15	1.41 ± 0.37	1.91 ± 0.62	0.63 ± 0.05	0.63 ± 0.07	1.70 ± 0.52	0.08 ± 0.05	0.10 ± 0.07	**360.7 ± 24.3**	313.4 ± 84.2	317.5 ± 115.0
	Map 6-1	*23*	*1.40 ± 0.25*	*1.66± 0.08*	*0.62 ± 0.02*	*0.59 ± 0.02*	*1.43 ± 0.11*	*0.08 ± 0.03*	*0.09 ± 0.03*	*365.3 ± 7.3*	***266.0 ± 24.27***	***258.3 ± 25.0***
	Map 6-2	*82*	*1.45 ± 0.11*	*1.78± 0.06*	*0.63 ± 0.01*	*0.62 ± 0.01*	*1.64 ± 0.07*	*0.06 ± 0.01*	*0.07 ± 0.01*	***358.9± 3.02***	*306.7 ± 12.3*	*304.4 ± 15.2*
4	Punctual	13	1.25 ± 0.20	1.82 ± 0.12	0.64 ± 0.02	0.61 ± 0.02	1.59 ± 0.12	0.10 ± 0.03	0.08 ± 0.03	356.6 ± 8.4	**297.6 ± 21.7**	293.6 ± 26.1
	Map	*1225*	*1.35 ± 0.12*	*1.77± 0.05*	*0.63 ± 0.01*	*0.61 ± 0.01*	*1.56 ± 0.07*	*0.08 ± 0.01*	*0.08 ± 0.01*	*352.7 ± 2.8*	***292.3 ± 13.6***	*287.1 ±15.9*
5	Punctual	14	1.31 ± 0.17	1.83 ± 0.23	0.64 ± 0.02	0.61 ± 0.02	1.56 ± 0.09	0.09 ± 0.03	0.08 ± 0.04	356.8 ± 9.0	**296.4 ± 28.6**	292.3 ± 35.0

	Map	*111*	*1.29 ± 0.06*	*1.81 ± 0.03*	*0.64 ± 0.004*	*0.62 ± 0.01*	*1.62 ± 0.04*	*0.08 ± 0.01*	*0.08 ± 0.01*	*350.3 ± 2.0*	***302.4 ± 8.1***	*299.2 ± 9.8*
3	Punctual	15	1.11± 0.34	2.10 ± 0.79	0.64 ± 0.05	0.58 ± 0.11	1.46 ± 0.61	0.17± 0.11	0.12 ± 0.05	356.1 ± 21.6	263.8 ± 133.3	263.7 ± 135.6
	Map	*1758*	*0.95 ± 0.16*	*1.77± 0.38*	*0.62± 0.03*	*0.60 ± 0.05*	*1.51 ± 0.28*	*0.10 ± 0.14*	*0.05 ± 0.09*	*357.3 ± 12.8*	*280.1 ± 57.2*	*275.5 ± 61.2*

Table 2